Broadband Analytical Magnetoquasistatic Electromagnetic Induction Solution for a Conducting and Permeable Spheroid

Benjamin E. Barrowes *Student Member, IEEE,* Kevin O'Neill *Member, IEEE*,
Tomasz M. Grzegorczyk *Member, IEEE*, Xudong Chen, and Jin A. Kong *Fellow, IEEE*

***Abstract*— We use a hybrid model including asymptotic expressions of the spheroidal wave functions (SWFs) to obtain a reliable, broadband solution for the electromagnetic induction (EMI) response from a conducting and permeable spheroid. We obtain this broadband response, valid in the magnetoquasistatic regime from 0 Hz to 100's of kHz, by combining three different techniques each applicable over a different frequency range. At low frequencies, the exact analytical solution is used. At mid-range frequencies, asymptotic expressions for the angular and radial SWFs are implemented to maintain a stable solution for the induced magnetic field. At higher frequencies, a small penetration approximation (SPA) solution is used when the SPA solution approaches the asymptotic assisted solution to within some predefined tolerance. Validation of this combined technique is accomplished by comparison of the induced magnetic field predicted by our model to both a finite element/boundary integral (FE-BI) numerical solution and experimental data from various spheroids taken by an ultra-wideband EMI instrument.**

***Index Terms*— electromagnetic induction, spheroidal wave functions, asymptotic expansion, small penetration approximation**

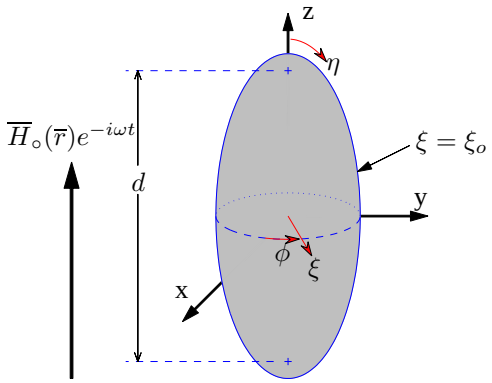

Fig. 1. Spheroidal Geometry: $1 \leq \xi < \infty$ (Oblate case: $0 \leq \xi < \infty$), $-1 \leq \eta \leq 1$, $0 \leq \phi \leq 2\pi$, $x = \frac{d}{2}[(1 \mp \eta^2)(\xi^2 \mp 1)]^{\frac{1}{2}} \cos(\phi)$, $y = \frac{d}{2}[(1 \mp \eta^2)(\xi^2 \mp 1)]^{\frac{1}{2}} \sin(\phi)$, $z = \frac{d}{2}\eta\xi$, $e = \frac{b}{a}$, $\xi = \left(\pm(1-e^{-2})\right)^{-\frac{1}{2}}$, $d = 2\left(\pm(b^2-a^2)\right)^{\frac{1}{2}}$. Upper sign $\rightarrow$ prolate, lower sign $\rightarrow$ oblate.

I. Introduction

ELECTROMAGNETIC induction (EMI) techniques have long been important in geophysical surveying [1]–[3]. In the past ten years or so, intense interest has focused on small ultrawide band (UWB) electromagnetic induction (EMI) (10's of Hz up to 100's of kHz) sensors used for shallow surveying to detect and discriminate metallic objects with one principal application being the detection and discrimination of unexploded ordnance (UXO) [4]–[8]. UXO contaminate wide regions of the globe and render those regions dangerous at best and uninhabitable at worst [9]–[11]. Typical UXO are nonspherical, however, thus complicating the detection and discrimination process.

While the solution for the induced magnetic field and potential within and around a conducting and permeable sphere under time harmonic excitation were first proposed by Wait [12], [13] over fifty years ago, lack of an analytical magnetoquasistatic solution for nonspherical shapes has hampered development of appropriate signal processing, inversion, and even instrument calibration. Recently some important progress has been made in formulating and evaluating spheroidal EMI solutions [14], [15]. While special approximations resolved evaluation problems at high EMI frequencies, and the full analytical formulation worked well at low EMI frequencies, stability problems persisted in the mid-frequency range, depending on the geometrical and material properties of the spheroid. To remedy this, we construct a combined solution for the induced magnetic field from metallic spheroids that applicable over the entire EMI band, for both oblate and prolate spheroidal shapes.

Our combined system incorporates asymptotic approximations of the angular and radial spheroidal wave functions [16] (ASWFs and RSFWs) into these existing low and high frequency solutions [14] for the induced magnetic field. This extends the frequency range over which the induced magnetic field external to the spheroid may be obtained to cover the problematical mid-frequency range. To be more specific, "low" frequency generally refers to frequencies ranging from static to frequencies below the resonant peak of the phase quadrature response of the induced magnetic field. "High" EMI frequencies are those at which the skin depth of the metallic object is very small relative to its dimensions. As frequency increases further into this "high" frequency range, the EMI

Benjamin E. Barrowes, Tomasz M. Grzegorczyk, Xudong Chen, and Jin A. Kong are with the Research Laboratory of Electronics and Department of Electrical Engineering and Computer Science, Massachusetts Institute of Technology, Cambridge, MA 02139-4307

Kevin O'Neill is with the United Stated Army Corps of Engineers ERDC, 72 Lyme Road, Hanover, New Hampshire, USA 03755-1290

This work was supported by the Strategic Environmental Research and Development Program and the United Stated Army Corps of Engineers ERDC UXO EQT program.

response asymptotically approaches the high frequency limit of vanishing internal magnetic field and the object acts as a perfect (EMI) reflector.

Section II contains a brief review of the formulation for the exact solution for the magnetic field within and around a conducting and permeable spheroid under time harmonic excitation, valid at small size parameters (or frequencies). Section III-A presents an asymptotic-assisted analytical solution based on known asymptotic expansions [16] of the spheroidal wave functions (SWFs). One other approach proposed in the literature to bridge this frequency gap is to implement a rational function approximation [15] which is based on the singular expansion method (SEM) [17]. However, this solution is neither rigorous nor exact, and can yield incorrect results for underdetermined systems. Our asymptotic-assisted solution realizes all higher order terms for mid-frequencies until it too encounters numerical difficulties for higher frequencies. A small penetration approximation (SPA) is then used to find the solution for the external induced magnetic field at high frequencies for which the exact and asymptotic-assisted solutions do not converge. This SPA solution is summarized in Section III-B.

Results for the induced magnetic field from a conducting and permeable spheroid are compared to both Wait's solution (in the particular case of the sphere) as well as to a finite element/boundary integral (FE-BI) numerical solution [18] in the case of a spheroid, in Section IV-A. In Section IV-B, the induced fields predicted by our combined method are compared to ultrawide band (UWB) data obtained with the Geophex GEM-3 [19] instrument, for prolate and oblate, permeable (magnetic) and non-permeable machined spheroids. Model and data are found it to be in excellent agreement if the permeability and conductivity of the spheroids are allowed to vary within acceptable physical ranges. Results illustrate that solutions are distinct based on spheroid characteristics and orientation. On this basis, our method could become the forward problem component on which inversion schemes may be based.

II. Exact Formulation

The formulation for the exact analytical solution for the induced magnetic field from a conducting and permeable spheroid under time harmonic excitation in the magnetoquasistatic regime is given in [14] and will only be summarized here.

Let a spheroid with high conductivity σ and relative permeability μ_r (as compared to the background medium) be excited by a time harmonic primary field $\overline{H}_\circ(\overline{r})e^{-\mathrm{i}\omega t}$ (time dependence expression $e^{-\mathrm{i}\omega t}$ is suppressed below). We assume the background medium is homogeneous, only weakly magnetic, and poorly conducting so that the wavenumber, $k_\circ$, of the host medium may be approximated by $k_\circ \approx 0$. As a result of this magnetoquasistatic approximation [3], the primary magnetic field, $\overline{H}_\circ(\overline{r})$, and the induced (or secondary) external magnetic field, $\overline{H}_\mathrm{s}(\overline{r})$, are irrotational and can be described by scalar potentials, $U_\circ(\overline{r})$ and $U_\mathrm{s}(\overline{r})$ respectively which both satisfy the Laplace equation in spheroidal coordinates. The known primary field potential can be expanded in terms of solutions of the first kind of the Laplace equation in spheroidal coordinates

$$U_\circ(\overline{r}) = H_\circ \frac{d}{2} \sum_{m=0}^{\infty} \sum_{n=m}^{\infty} \sum_{p=0}^{1} b_{pmn} P_n^m(\eta) P_n^m(\xi) T_{pm}(\phi), \quad (1)$$

where $P_n^m(\beta)$ represents the associated Legendre function of the first kind of degree n and order m [20]. Similarly, the secondary field potential can be expanded in terms of Laplace solutions of the second kind as

$$U_\mathrm{s}(\overline{r}) = H_\circ \frac{d}{2} \sum_{m=0}^{\infty} \sum_{n=m}^{\infty} \sum_{p=0}^{1} B_{pmn} P_n^m(\eta) Q_n^m(\xi) T_{pm}(\phi), \quad (2)$$

where $Q_n^m(\beta)$ represents the associated Legendre function of the second kind of degree n and order m [20] and B_{pmn} are unknown secondary induced field expansion coefficients. The total external magnetic field is the sum of the primary and secondary fields

$$\overline{H}_2 = \overline{H}_\circ + \overline{H}_\mathrm{s} = -\nabla U_\circ - \nabla U_\mathrm{s}. \quad (3)$$

Within the highly conducting object, the internal magnetic field of the spheroid, $\overline{H}_1(\overline{r})$, can be found by solving the vector wave equation in spheroidal coordinates

$$\nabla \times \nabla \times \overline{H}_1(\overline{r}) - k_1^2 \overline{H}_1(\overline{r}) = 0 \quad (4)$$

where $k_1^2 = \mathrm{i}\omega\sigma_1\mu_1$. Under these assumptions, the Helmholtz equation above becomes a diffusion equation. $\overline{H}_1(\overline{r})$ can be expressed as an infinite series of vector spheroidal wave functions (VSWFs) $\overline{M}$ and $\overline{N}$ as

$$\overline{H}_1 = H_o \sum_{m=0}^{\infty} \sum_{n=m}^{\infty} \sum_{p=0}^{1} \left[A_{pmn}^{(M)} \overline{M}_{pmn}^{r(1)}(c_1;\eta,\xi,\phi) + A_{pmn}^{(N)} \overline{N}_{pmn}^{r(1)}(c_1;\eta,\xi,\phi) \right] \quad (5)$$

where the size parameter, c, of a spheroid is defined as

$$c = \frac{k_1 d}{2}, \quad (6)$$

k_1 is the wavenumber inside the spheroid, and d is the interfocal distance.

$\overline{M}_{pmn}^{r(1)}(c_1;\eta,\xi,\phi)$ and $\overline{N}_{pmn}^{r(1)}(c_1;\eta,\xi,\phi)$ are in turn composed of the angular and radial SWFs, $S_{mn}(c,\eta)$ and $R_{mn}(c,\xi)$ [21] as well as the harmonic functions $T_{pm}(\phi)$ defined as

$$T_{pm}(\phi) = \begin{cases} \cos(m\phi) & \text{p=0,} \\ \sin(m\phi) & \text{p=1.} \end{cases} \quad (7)$$

The exact solution for $\overline{H}_\mathrm{s}$ can be obtained by matching the tangential magnetic fields, $\overline{H}_\eta$ and $\overline{H}_\phi$, and the normal component of the magnetic flux density, $\overline{B}_\xi$, at the surface of the spheroid, i.e.

$$H_{1\eta} = H_{2\eta} \quad (8a)$$

$$\mu_r H_{1\xi} = H_{2\xi} \quad (8b)$$

$$H_{1\phi} = H_{2\phi} \quad (8c)$$

where $\mu_r = \mu_1/\mu_2$ is the relative permeability of the spheroid compared to the surrounding medium. Substituting (1)–(6)

into (8) results in an infinite set of equations which must be massaged, truncated, and then cast into matrix form in order to be solved [14].

Even though this solution for the induced magnetic field from a conducting and permeable spheroid is theoretically applicable for any frequency satisfying the magnetoquasistatic assumptions, two problems limit the practical applicability of this solution. The first is that the basis functions used to express the magnetic field internal to the spheroid, in this case the angular (ASWF) and radial (RSWF) spheroidal wave functions, $S_{mn}(c,\eta)$ and $R_{mn}(c,\xi)$ respectively, are in general not orthogonal to each other for different m, n, and c as are the spherical wave functions. Because of this, the complexity of the solution is increased due to the infinite sets of equations arise when matching the boundary conditions at the spheroidal surface.

The second, more challenging difficulty is that the angular and radial SWFs, which must be evaluated as part of $\overline{M}_{pmn}^{r(1)}(c_1;\eta,\xi,\phi)$ and $\overline{N}_{pmn}^{r(1)}(c_1;\eta,\xi,\phi)$, become unstable at moderate size parameters (or frequencies) on the order of $|c| \approx 30$ [14], [21]. This tendency to diverge is shown qualitatively in Section IV-A Fig. 3 where the frequencies to the left of the first dashed vertical line indicate the limited region of stability of the exact method. This numerical difficulty is typically encountered at frequencies lower than that where the resonant peak of the response is fully developed. Some other method is therefore desirable, to extend the range of frequencies over which solutions for the induced magnetic field are tractable . In the next section, we implement asymptotic expansions of the SWFs in order to extend the solution's range of stability to higher frequencies. However, the size parameter c for the wave (in this case, diffusion) equation is complex (see Section II), and asymptotic expansions of the SWFs for the case of complex size parameter have not been treated extensively in the literature (for a summary, see [16]).

III. High Frequency Approximations

A. Asymptotic Expressions for the Spheroidal Wave Functions

We use asymptotic expansions of the spheroidal wave function for complex size parameter c [16], [22] to extend the range over which the full analytical solution is stable to larger c than previously possible. Through the use of these asymptotic expansions, the maximum c for which the full analytic solutions is stable is increased closer to the size parameter for which the small penetration approximation (SPA [14], see Section III-B) is valid. Accordingly, the accuracy of the induced field solution for this mid-frequency range is on the same order as the accuracy of the asymptotic expansions. Unfortunately, some aspect of this asymptotic-assisted solution also becomes numerically unstable at a frequency that is a function of the relative permeability, μ_r, the overall dimensions a and b of the spheroid, and the aspect ratio $e = b/a$.

The original Legendre and Bessel function expansions for the ASWF and RSWF respectively become unstable in double precision for size parameters larger than $|c| \approx 30$ [14], [21]. Consequently, the full analytic solution outlined in Section II fails to converge for spheroidal size parameters beyond this range. For these larger c, asymptotic expansions of the SWFs do exist which remain stable. However, these established asymptotic expansions traditionally treat only the cases of purely real (for the case of the prolate SWFs) or purely imaginary (oblate SWFs) size parameter [16], [21], [23], [24].

	exp.	m=0		exp.	m=1		exp.	m=2	
$(n-m)$	type	n_p	n_o	type	n_p	n_o	type	n_p	n_o
0	Pro.	0	-	Pro.	1	-	Pro.	2	-
1	Obl.	-	0	Pro.	2	-	Pro.	3	-
2	Obl.	-	1	Obl.	-	1	Pro.	4	-
3	Pro.	1	-	Obl.	-	2	Obl.	-	2
4	Pro.	2	-	Pro.	3	-	Obl.	-	3
5	Obl.	-	2	Pro.	4	-	Pro.	5	-
6	Obl.	-	3	Obl.	-	3	Pro.	6	-
7	Pro.	3	-	Obl.	-	4	Obl.	-	4
8	Pro.	4	-	Pro.	5	-	Obl.	-	5
⋮		⋮			⋮			⋮	

TABLE I

Pattern governing n_p, n_o and which type of asymptotic expansion, either the *prolate*-type (Pro. above) or the *oblate*-type (Obl. above), for different combinations of m and n. c is of the form $c = (1+\mathrm{i})\,\alpha$.

When c is complex, asymptotic representations of the prolate SWFs (for prolate spheroids) and the oblate SWFs (for oblate spheroids) consist of either the *prolate*-type or *oblate*-type asymptotic expansions [16]. The choice of which type of asymptotic expansion is appropriate is determined by the spheroidal parameters m, n, and the size parameter c through a comparison of $\arg(c)$ to a look up table containing the branch points, $c_{\circ;r}^{mn}$ of the spheroidal wave equation. These branch points are found once through polynomial estimation techniques followed by a Newton-Raphson multivariable root finding method and stored for reference [16]. $c_{\circ;r}^{mn}$ for $0 \leq m \leq n \leq 110$ have been found, but for the purposes of this work, only $m \leq 1$, $n \leq 60$ are used. The diffusion equation, (4), dictates $\arg(c) = \pi/4$, for which a simple pattern, alternating between the *prolate* and *oblate* expansion types soon develops. Beginning at $n = m$, this pattern consists of $m+1$ *prolate*-type expansions followed by alternating pairs of *oblate* then *prolate*-type expansions.

When computing the *prolate*-type and *oblate*-type asymptotic expansions of the spheroidal eigenvalues, λ_{mn}, (and $S_{mn}(c,\eta)$, denoted $\lambda_{mn}^{(a)}$ and $S_{mn}^{(a)}(c,\eta)$ respectively) for complex c, the ordering is different from the ordering, according to n, of the eigenvalues themselves. While the n indicates λ_{mn} ordering for each m, the $\lambda_{mn}^{(a)}$ are ordered according to m, but independently, corresponding to the sequential ordering for each type of expansion separately. Let n_p be the number of *prolate*-type expansions of λ_{mn} necessary, up to but excluding n, and n_o be the number of *oblate*-type expansions of λ_{mn} necessary, up to but excluding n. λ_{mn} can then be approximated by *prolate*-type $\lambda_{mn}^{(a)}$ ordered according to n_p beginning at $n_p = m$, and *oblate*-type $\lambda_{mn}^{(a)}$ ordered according to n_o beginning at $n_o = m$. This behavior can clearly be seen in Fig. 2, is summarized in Table I, and can be succinctly

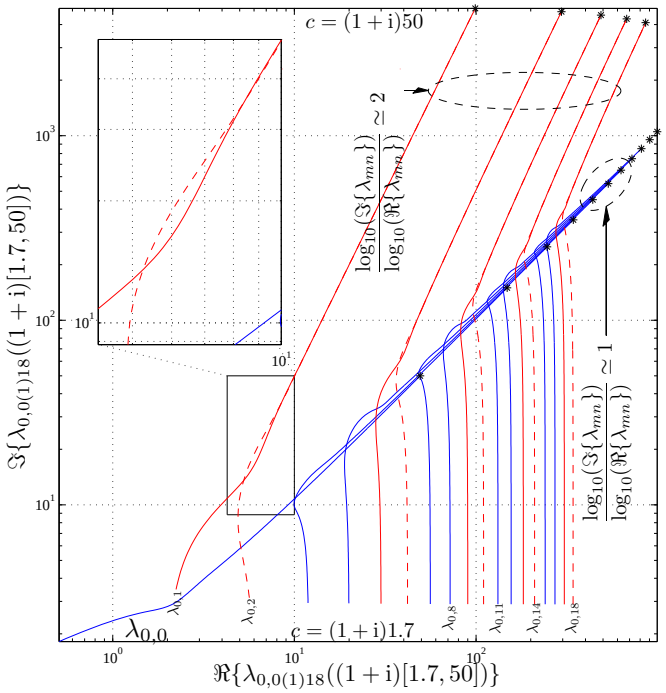

Fig. 2. λ_{mn}: Eigenvalues of the spheroidal wave equation. $m = 0$ and $n = 0(1)18$. Each curve tracks an eigenvalue as c ranges from $c = (1+\mathrm{i})1.7$ (lower end of each curve) to $c = (1+\mathrm{i})50$ (upper end of each curve). Dashed curves indicate coalescing oblate eigenvalue pairs.

written as [16]

$$n_p = \begin{cases} n, & (n-m) \le m \\ \left\lfloor \frac{(n-m)-m}{2} \right\rfloor + m + m, & (n-m) > m \end{cases} \tag{9}$$

and

$$n_o = \left\lfloor \frac{(n-m)-m}{2} \right\rfloor + m, \tag{10}$$

where $\lfloor\ \rfloor$ denotes the floor function.

The *prolate*-type asymptotic expansion of the angular SWF, $S^{(a)}_{mn}(c,\eta)$, used in this work is found by expanding $S_{mn}(c,\eta)$ in terms of an infinite series of the form,

$$S_{mn}(c,\eta) \approx S^{(a)}_{mn}(c,\eta) = (1-\eta^2)^{\frac{m}{2}} \sum_{r=-\infty}^{\infty}{}' C_r D_{n_p-m+r}(x) \tag{11}$$

where $D_{n_p-m+r}(x)$ is the parabolic cylinder function of order (n_p-m+r) [20] (note the dependence on n_p), the prime indicates summation over even r, and C_r are expansion coefficients [16], [21], [23]. The eigenvalues in this case are expanded in an inverse power series as

$$\lambda_{mn} \approx \lambda^{(a)}_{mn} = \sum_{k=0}^{\infty} \Gamma_k(m,n_p) c^{-k+1} \tag{12}$$

where the functional dependence of the expansion coefficients Γ_k has been made explicit. C_r and $\Gamma_k(m,n_p)$ are found by substituting (11) and (12) into the spheroidal wave equation [23].

If a given combination of m, n, and $\arg(c)$ requires an *oblate*-type asymptotic expansion for $S_{mn}(c,\eta)$, it is expressed as an infinite series of associated Laguerre polynomials, $L^{(m)}_{\nu+r}(x)$ [20], [25],

$$S^{(a)}_{mn}(-\mathrm{i}c,\eta) = (1-\eta^2)^{\frac{m}{2}} \sum_{r=-\nu}^{\infty} A_r \left\{ e^{-c(1-\eta)} L^{(m)}_{\nu+r}\left[2c(1-\eta)\right] + (-1)^{n-m} e^{-c(1+\eta)} L^{(m)}_{\nu+r}\left[2c(1+\eta)\right] \right\}, \tag{13}$$

where A_r are expansion coefficients and $\nu = \left\{ \begin{smallmatrix} (n_o-m)/2 \\ (n_o-m-1)/2 \end{smallmatrix} \right\}$ when (n_o-m) is $\left\{ \begin{smallmatrix} \text{even} \\ \text{odd} \end{smallmatrix} \right\}$ [16], [21], [24]. The inverse power series representation for λ_{mn} now becomes

$$\lambda_{mn} = \sum_{k=0}^{\infty} \Gamma_k(m,n_o)(-\mathrm{i}c)^{-k+2}. \tag{14}$$

where $\Gamma_k(m,n_o)$ are expansion coefficients. In a manner similar to that used in the case of the *prolate*-type asymptotic expansion, A_r and $\Gamma_k(m,n_o)$ for the *oblate*-type asymptotic expansion can be found by substituting (13) and (14) into the spheroidal wave equation [24].

The original expansion for radial SWFs in terms of an infinite series of spherical Bessel functions also becomes inaccurate for large c [21]. Fortunately, the RSWFs adhere to the same pattern of asymptotic expansion types as in the case of the ASWFs. Additionally, $S_{mn}(c,\eta)$ and $R_{mn}(c,\xi)$ are proportional for a given c, i.e.

$$S^{(i)}_{mn}(c,\eta) = \kappa^{(i)}_{mn}(c) R^{(i)}_{mn}(c,\eta) \tag{15}$$

where the superscript (i) indicates the *kind* of the SWF [21]. For the *prolate*-type asymptotic expansion of $R_{mn}(c,\xi)$, we use Equation (3.11) in Miles [26]. For the *oblate*-type asymptotic expansion of the RSWF, we use (15) because $S^{(a)}_{mn}(-\mathrm{i}c,\eta)$ is much better behaved and suffers from fewer numerical problems for $|\eta| > 1$.

B. Small Penetration Approximation

For much higher frequencies which approach the limit of vanishing internal magnetic field, a small penetration approximation (SPA) for the internal magnetic field, $\overline{H}_1(\overline{r})$, has been developed [14], [27]. According to the SPA, the ξ-dependence of the azimuthal component of the internal magnetic field, $H_{1\phi}$, is approximated as a decaying exponential, $e^{-\mathrm{i}k_1 h_\xi \xi}$, leading to a self-consistent equation relating the internal fields of the spheroid at the boundary. Using the boundary conditions of (8), $\overline{H}_1$ can then be expressed in terms of the components of $\overline{H}_2(\overline{r})$, thus avoiding any reference to the SWFs and the accompanying computational difficulty. This approach yields stable solutions for very large c, up into the frequency range in which the magnetic field inside the spheroid becomes negligible as it approaches the high frequency limit of zero field. In this frequency range, and the induced field can be well modeled as a dipole response from a perfect EMI reflector.

This SPA solution applies at very high frequencies, but has also been found to be moderately accurate for lower frequencies, especially for highly permeable objects. In anticipation of the non-convergence of the asymptotic-assisted solution, both

solutions are calculated over the entire frequency range. If the asymptotic-assisted solution remains convergent for frequencies at which the SPA solution is sufficiently accurate (arbitrarily set to some predefined tolerance), a seamless switchover to the SPA solution occurs. If instead the asymptotic-assisted solution fails to converge before some suitable switchover criterion is satisfied, the asymptotic-assisted solution is abandoned and the SPA solution is adopted regardless. We choose the switchover frequency to be the frequency at which the dipole term of the asymptotic-assisted solution of the induced field is within some small error, B^{δ}_{0m1}, of the dipole term of the corresponding SPA solution in the asymptotic regime,

$$B^{\delta}_{0m1} = \left| \frac{B_{0m1} - B^{spa}_{0m1}}{B^{spa}_{0m1}} \right| \tag{16}$$

where $m = 0$ for axial excitation, and $m = 1$ for transverse excitation. For spheroids with $1 \leq \mu_r \leq \infty$ and $\frac{1}{8} \leq \mu_r \leq 8$, the asymptotic-assisted solution switches over to the SPA solution when B^{δ}_{0m1} is less than 5%. In the vast majority of cases, B^{δ}_{0m1} is less than 2% with only more extreme aspect ratios and slightly magnetic objects posing the most difficulty.

IV. Validation and Results

A. Comparison with Simulation

The induced magnetic field potential and hence the magnetic field can be calculated anywhere external to the spheroid through (2) after the induced potential expansion coefficients B_{pmn} are found from the combined solution outlined in the previous sections. In this section, we compare this solution with results from both Wait's solution for a conducting and permeable sphere [12] and to results obtained from a hybrid solution based on a finite element/boundary integral method (FE-BI) combined with a thin skin approximation [18]. We compare both the axial ($m = 0$) and transverse ($m = 1$) excitations of prolate and oblate spheroids. For axial excitation, the primary field is aligned with the laboratory z-axis $\overline{H}_{\circ}(\overline{r}) = \hat{z}$, the axis of rotation of the spheroid is aligned with the z-axis, and $b_{001} = -1$ in (1) with all other $b_{00n} = 0$. In the case of transverse excitation, we choose to rotate the spheroid (as opposed to the laboratory reference frame) so that the spheroid is aligned with the x-axis while the primary magnetic field is still $\overline{H}_{\circ}(\overline{r}) = \hat{z}$ mandating $b_{011} = 1$ with all other $b_{01n} = 0$. Following this convention, the Cartesian coordinates refer to the laboratory reference frame. The spheroid's location is then expressed in terms of this Cartesian system, while its orientation relative to the laboratory is referenced using the three Euler angles $\{\alpha, \beta, \gamma\}$ [28].

In all cases considered here, even at the "high" frequencies, we assume that electromagnetic phenomena are magnetoquasistatic in the sense that displacement currents are negligible. Within the metallic object, the ratio of conduction to displacement currents is $\sigma/(\omega\varepsilon)$. Even at a frequency of 100 MHz (as shown in Figs. 3–5), this is $\approx 10^7/(10^8 10^{-11})$, so that conduction currents dominate by orders of magnitude [29], [30]. Accordingly, even at EMI frequencies above 1 MHZ, there is essentially no phase difference between one observation point and another within the length scale of interest (meters). External fields appear static, being time dependent only as they follow imposed boundary conditions.

When the asymptotic representations of the SWFs outlined in Section III are utilized to find $\overline{H}_2(\overline{r})$, the solution is indeed stable for higher frequencies, as can be seen in Fig. 3, which shows combined results calculated by all three techniques outlined in this paper, viz. original exact solution, asymptotic-assisted solution, and the SPA solution. This combined solution is capable of finding the induced secondary magnetic field over a broad EMI frequency range from static to very high frequencies.

Important characteristics of the broadband EMI response are illustrated in Figs. 3–5. For these comparisons, the center of all of the spheroids were 30cm below the measurement point and under uniform excitation $\overline{H}_{\circ} = \hat{z}$. For all the results reported in this work, our choice of sign convention follows the convention common in the geophysics field in that the conjugate of the magnetic field is shown.

In Fig. 3, as the aspect ratio decreases from $e = 6$ (prolate) to $e = 1/6$ (oblate), the resonant peak of the induced field shifts to higher frequencies under axial excitation. Simultaneously, the frequency at which $|\Re\{H_{sz}\}| = |\Im\{H_{sz}\}|$ shifts from higher to lower frequencies. Figure 4 shows $\overline{H}_2(\overline{r})$ for the same five spheroids considered in Fig. 3 except that they are under transverse excitation, i.e. the spheroids' axes of revolution are aligned with the x-axis, with the same primary field, $\overline{H}_{\circ}(\overline{r}) = \hat{z}$. Both Wait's solution ($e = 1$) and the numerical solution are included for reference. The resonant peak of $|\Im\{H_{sz}\}|$ is essentially equal for the sphere and two oblate spheroids. This is because the dimension of these objects that is aligned with the primary field ($\hat{z}$ in this case) is the same. This dependence of the induced field on object orientation could aid in object discimination, especially if multiple measurements from different locations are considered.

Figure 5 compares the combined analytical solution to solutions from the same numerical method for spheroids with aspect ratio $e = 3$ and $\mu_r = [1, 5, 10, 50, 100]$. Note that with the spheroids' dimensions equal, the high frequency limits of all the spheroids in Fig. 5 are identical because the spheroids act as identical EMI reflectors. However, the static limit, which limit depends principally on the object's volume, and the peak and crossover frequencies are characteristic of each spheroid. The distinct progression of the crossover point to lower frequencies as the permeability decreases is noteworthy.

For the spherical cases shown, the aspect ratio used for the combined method is slightly different from 1.0 (in this case 1.005) because $R_{mn}(c, \xi)$ possesses a singularity at $e = 1$ ($\xi = \infty$). Wait's solution is obscured by our analytical model. Results from our combined model, Wait's solution, and the FE-BI numerical method are essentially equal.

B. Comparison with Measurements

In this section we compare our results from the combined broadband method to measurements taken in the frequency domain using the UWB GEM-3 instrument [19]. For nonuniform primary fields such as those produced by the GEM-3 that

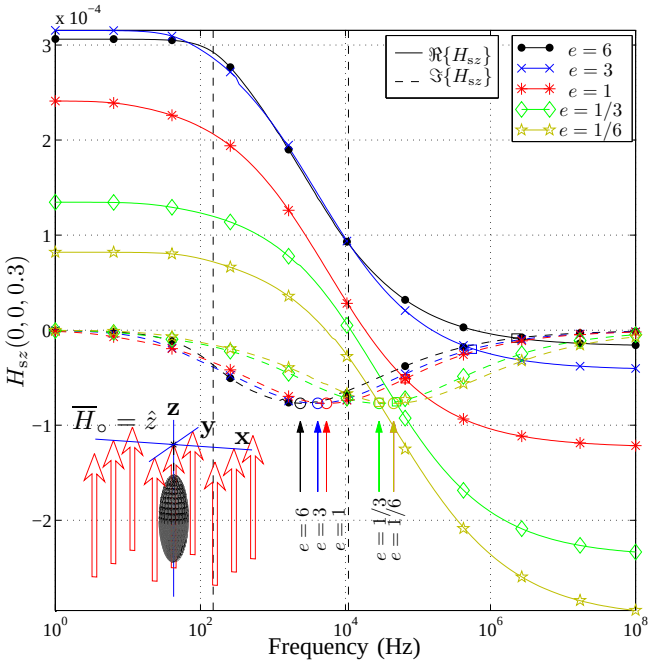

Fig. 3. z-component of the induced secondary field, H_{sz}, from five different spheroids, aspect ratio $e = [6, 3, 1, 1/3, 1/6]$, with their longest dimension equal to 3cm, and axial excitation calculated by the combined method described in Sections II and III. $\sigma = 10^7$ and $\mu_r = 100$. Vertical dashed lines give a rough indication of the regions of validity for the exact, asymptotic-assisted, and SPA solutions, progressing from low to high frequency. Circles (and arrows) indicate the resonant peak of $\Im\{H_{sz}\}$. Squares indicate the frequencies at which $|\Re\{H_{sz}\}| = |\Im\{H_{sz}\}|$. Markers indicate results from the corresponding numerical solution [18]. Note that H_{sz} has been normalized so that $\max(|\Im\{H_{sz}\}|) = \max(|\Im\{H_{sz}^{\text{sphere}}\}|)$.

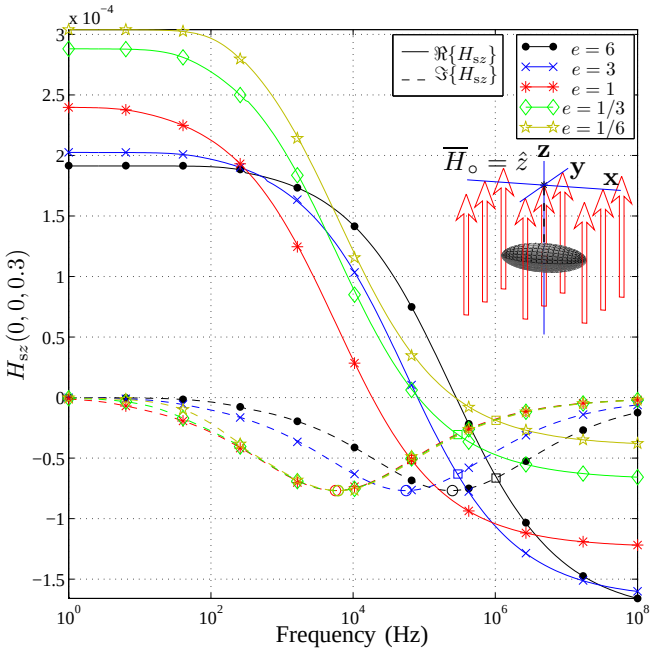

Fig. 4. H_{sz} from the same five spheroids as in Fig. 3 under transverse excitation. $\overline{H}_\circ = \hat{z}$ with spheroids' axes of revolution aligned along the x-axis. Again, H_{sz} has been normalized so that $\max(|\Im\{H_{sz}\}|) = \max(|\Im\{H_{sz}^{\text{sphere}}\}|)$.

still satisfy the magnetoquasistatic assumptions, $b_{0mn} \neq 0$ for $n \neq 1$. In order to find the induced external magnetic field from (2) and (3), the primary field from the GEM-3 must be expressed in terms of excitation coefficients b_{0mn}. The b_{0mn} are dependent upon the particular spheroidal coordinate system, (η, ξ, ϕ, d), and its orientation with respect to $\overline{H}_\circ(\overline{r})$.

One way to find these excitation coefficients is to utilize the orthogonality of the associated Legendre and harmonic functions in (1) in order to find an expression for b_{pmn} [20], i.e.

$$b_{pmn} = \frac{\int_0^{2\pi} T_{pm}(\phi) \int_{-1}^{1} P_n^m(\eta)\ U_\circ(\overline{r})\ d\eta\, d\phi}{\ell \pi H_\circ \frac{d}{2} \frac{P_n^m(\xi)}{(n+\frac{1}{2})} \frac{(n+m)!}{(n-m)!}}, \qquad (17)$$

where

$$\ell = \begin{cases} 2\pi\widetilde{p} & \text{m=0,} \\ \pi & \text{otherwise} \end{cases} \qquad (18)$$

with $\widetilde{p} = 1$ for $p = 0$ and vice versa. This assumes that the potential for the primary field is known at the surface of the spheroid. If $U_\circ(\overline{r})$ is unknown, $\overline{H}_\circ(\overline{r})$ may be used instead by taking $-\nabla$ of both sides of (1) and performing the same procedure as shown in (17). These expressions involve multiple integrals which must be performed numerically unless some convenient analytical representation of $U_\circ(\overline{r})$ or $\overline{H}_\circ(\overline{r})$ is known.

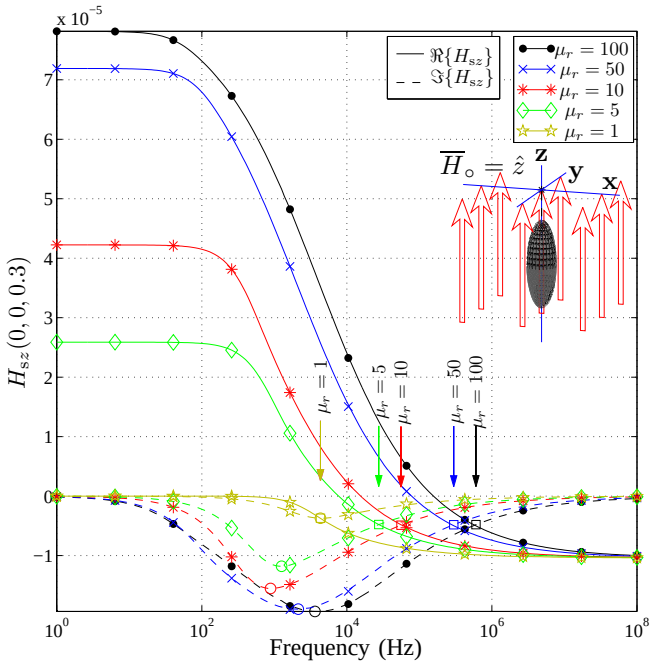

Fig. 5. H_{sz} from five spheroids under axial excitation with a similar configuration to that of Fig. 3, but with $\mu_r = [1, 5, 10, 50, 100]$, aspect ratio $e = 3$, and $2a = 3$cm. $\overline{H}_\circ = \hat{z}$. Arrows indicate frequencies at which $|\Re\{H_{sz}\}| = |\Im\{H_{sz}\}|$.

A simpler method, which avoids time consuming numerical integrations, for obtaining b_{pmn} is to use point matching in (1)

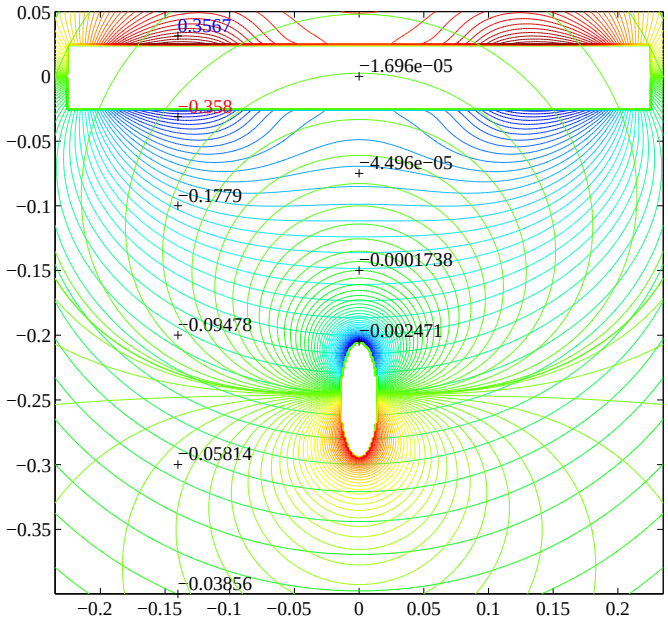

Fig. 6. Primary field potential from the GEM-3, $U_\circ(\overline{r})$ (magnitudes marked on left), and the secondary potential induced by the spheroid, $U_\mathrm{s}(\overline{r})$ (magnitudes marked in center) in the $x-z$ plane for the S2 spheroid (see Table II), at high frequency, under axial excitation, and choosing $\mu_r = 100$ and $\sigma = 10^7$. Color of induced response has been adjusted for clarity. Axes are in meters. The white rectangle encompasses the GEM-3 instrument.

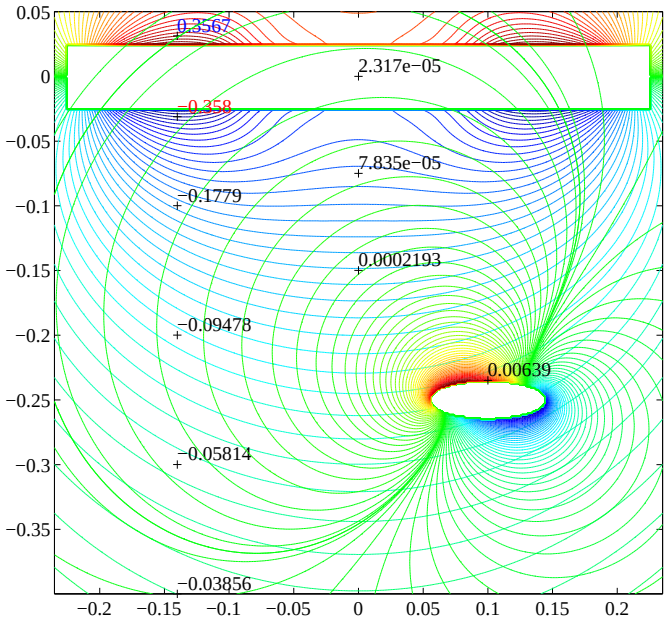

Fig. 7. Primary field potential from the GEM-3, $U_\circ(\overline{r})$ (magnitudes marked on left), and the secondary potential induced by the spheroid, $U_\mathrm{s}(\overline{r})$ (magnitudes marked in center) in the $x-z$ plane for the S2 spheroid (see Table II), at low frequency, under transverse excitation, offcenter, and choosing $\mu_r = 100$ and $\sigma = 10^7$. Color of induced response has been adjusted for clarity. Axes are in meters. The white rectangle encompasses the GEM-3 instrument.

at $N_p > 2(\max(m)+1)(\max(n)+1)$ points on the surface of the spheroid defined by $\xi = \xi_\circ$. The resulting system of equations resolves up to $N \leq N_p$ expansion coefficients again assuming some convenient expression for $U_\circ(\overline{r})$ or $\overline{H}_\circ(\overline{r})$ is known. This system of equations can be expressed as

$$\begin{bmatrix} U_\circ(\overline{r}_1) \\ U_\circ(\overline{r}_2) \\ \vdots \\ U_\circ(\overline{r}_{N_p}) \end{bmatrix} = \begin{bmatrix} \Phi_1(\overline{r}_1) & \Phi_2(\overline{r}_1) & \cdots & \Phi_N(\overline{r}_1) \\ \Phi_1(\overline{r}_2) & \Phi_2(\overline{r}_2) & \cdots & \Phi_N(\overline{r}_2) \\ \vdots & \ddots & \ddots & \vdots \\ \Phi_1(\overline{r}_{N_p}) & \Phi_2(\overline{r}_{N_p}) & \cdots & \Phi_N(\overline{r}_{N_p}) \end{bmatrix} \begin{bmatrix} b_1 \\ b_2 \\ \vdots \\ b_N \end{bmatrix} \tag{19}$$

where the potential at the i^{th} point on the surface is

$$\Phi_j(\overline{r}_i) \quad = \quad P_n^m(\eta_i) P_n^m(\xi_\circ) T_{pm}(\phi_i) \tag{20}$$

given some suitable mapping of $[p,m,n] \rightarrow j$. Equation (19) can easily be solved via (pseudo-) inversion or conjugate gradient techniques, yielding b_{pmn} in terms of the object's coordinates system. We adopt this approach, using an approximate representation of the GEM-3 primary field modeled as rings of magnetic sources [27]. Figure 6 depicts the primary and secondary induced potentials in the $x-z$ plane which includes both the center of the GEM-3 (assigned to be the origin) and a spheroid located at $\overline{r} = [0.0, 0.0, -0.25]$ meters. The spheroid's axis of symmetry is aligned with the z-axis in this case. Figures 6 and 7 illustrate the dramatic falloff in magnitude of the induced field as compared to the primary field. For these realistic cases, the induced field at the sensor is five orders of magnitude smaller than the primary field even though the object is at a relatively shallow depth.

For high but still magnetoquasistatic frequencies (see Fig. 6), the induced magnetic field will be out of phase with the primary field due to Lenz's law. Figure 7 shows $U_\circ(\overline{r})$ and $U_\mathrm{s}(\overline{r})$ for a low (near static) frequency case with the spheroid removed from the z-axis. In this case, the induced response in phase with the primary field.

We now compare the theoretical induced external magnetic field predicted by our combined broadband technique with the induced field measured by the GEM-3 instrument. The primary field and potential, $\overline{H}_\circ(\overline{r})$ and $U_\circ(\overline{r})$ respectively, at the surface of the spheroid are described by 12 rings of dipoles whose location and magnitudes are given by the method found in [27]. The primary field potential expansion coefficients, b_{pmn}, are then found via (19).

We machined a set of 17 spheroids for test objects: three spheres, six prolate spheroids, and eight oblate spheroids machined from aluminum and mild steel. Table II summarizes the spheroids' designations and characteristics, and they are pictured in Fig. 8. The induced magnetic fields for prolate steel spheroid S2 for both axial and transverse orientations are shown in Fig. 9. Figure 10 shows similar results for the aluminum spheroid A1 and Figs. 11 and 12 show similar comparisons for oblate spheroids S8 and A7 respectively. The measurements were taken from a position directly above each object.

The distance from the center of the receiver to the closest edge of each object was 25cm in the case of the steel objects, and 15cm in the case of the aluminum objects. Therefore, the distance to the center of S2 under axial orientation was $z = -34$cm, while the depth to the center under transverse

Fig. 8. Spheroid collection used for testing. Specifi cations are listed in Table II.

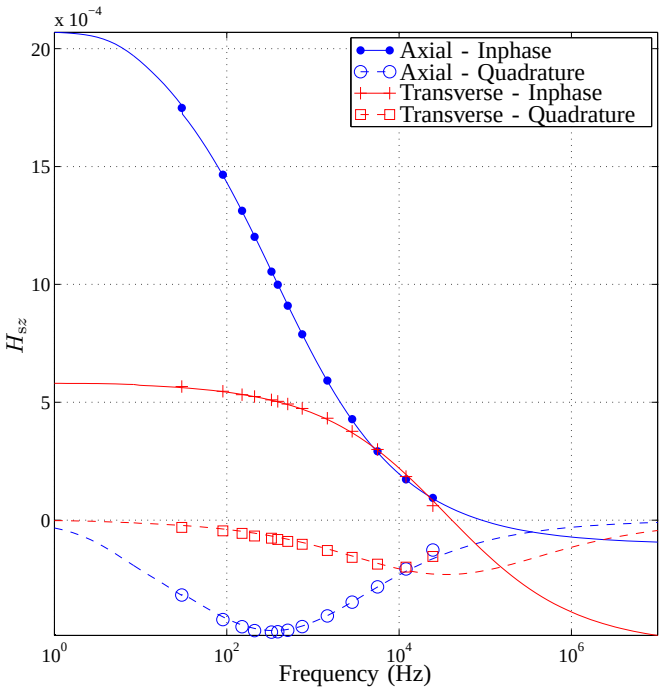

Fig. 9. Comparison of GEM-3 induced magnetic fi eld measurements, $H_{sz,d}$, from prolate steel spheroid S2 with combined model outlined in Sections II and III. Both axial and transverse cases are shown. Orientations are similar to those shown in plots of $U_s(\overline{r})$ such as Fig. 6. Optimized permeability and conductivity were $\mu_r = 234.1$ and $\sigma = 4.315 \times 10^6 \mho/m$, respectively.

orientation was $z = -26.5$cm, etc.

	comp.	type	semiaxis (a)	semiaxis (b)	nominal $e = b/a$
S1	Iron	sphere	90.62mm	90.62mm	1
S2	Steel	PS	30.02mm	182.19mm	6
S3	Steel	PS	29.94mm	90.28mm	3
S4	Steel	PS	14.97mm	90.76mm	6
S5	Steel	OS	29.32mm	4.56mm	1/6
S6	Steel	OS	29.59mm	9.65mm	1/3
S7	Steel	sphere	29.87mm	29.87mm	1
S8	Steel	OS	89.85mm	28.39mm	1/3
S9	Steel	OS	89.95mm	15.32mm	1/6
A1	Al	PS	30.17mm	180.23mm	6
A2	Al	PS	29.9mm	91.29mm	3
A3	Al	PS	15.04mm	91.14mm	6
A4	Al	OS	29.36mm	4.34mm	1/6
A5	Al	OS	29.36mm	8.88mm	1/3
A6	Al	sphere	29.91mm	29.91mm	1
A7	Al	OS	89.92mm	30.38mm	1/3
A8	Al	OS	89.98mm	15.94mm	1/6

TABLE II

PHYSICAL DIMENSIONS OF STEEL AND ALUMINUM SPHEROIDS. PS ⇒ PROLATE SPHEROID. OS ⇒ OBLATE SPHEROID.

Our implementation truncates the infinite sets of equations resulting from (8) at $m = 1$. This is partially due to the fact that at remote points in the "far field", or farther than one or two characteristic lengths (i.e. longest dimension of the object), the lower order, or $m = 0, 1$, terms of the induced magnetic field tend to dominate. Consequently, our solution includes effects for $m = 0$ and $m = 1$ only, which correspond to the axial and transverse excitations respectively [14]. Even with this limitation, the primary and secondary fields may be spatially nonuniform, however, because all n in the range $n \leq 60$ are considered. With reference to the GEM-3 primary

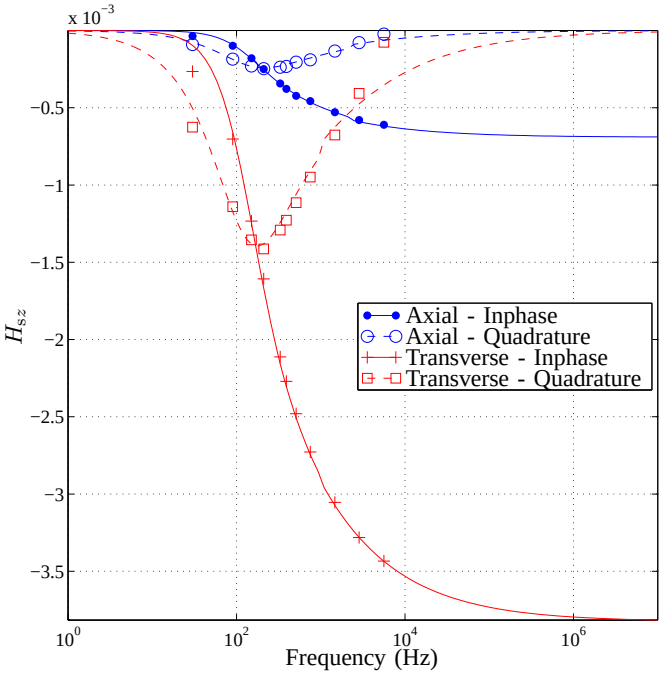

Fig. 10. Comparison of $H_{sz,d}$ from prolate aluminum spheroid A1 with combined model outlined in Sections II and III. Both axial and transverse cases. Optimized conductivity was $\sigma = 2.103 \times 10^7 \mho/m$.

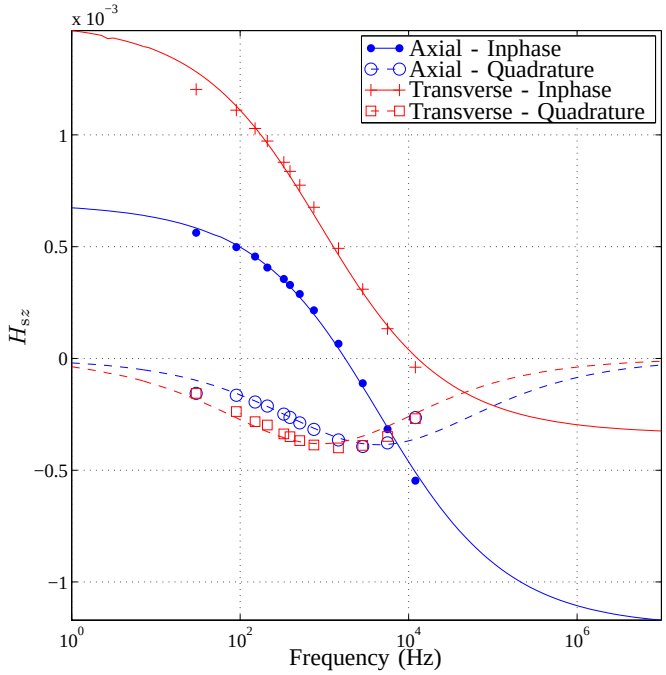

Fig. 11. Comparison of $H_{sz,d}$ from oblate steel spheroid S8 with combined model outlined in Sections II and III. Both axial and transverse cases. Optimized permeability and conductivity were $\mu_r = 268.0$ and $\sigma = 1.939\times10^7 \mho/m$, respectively.

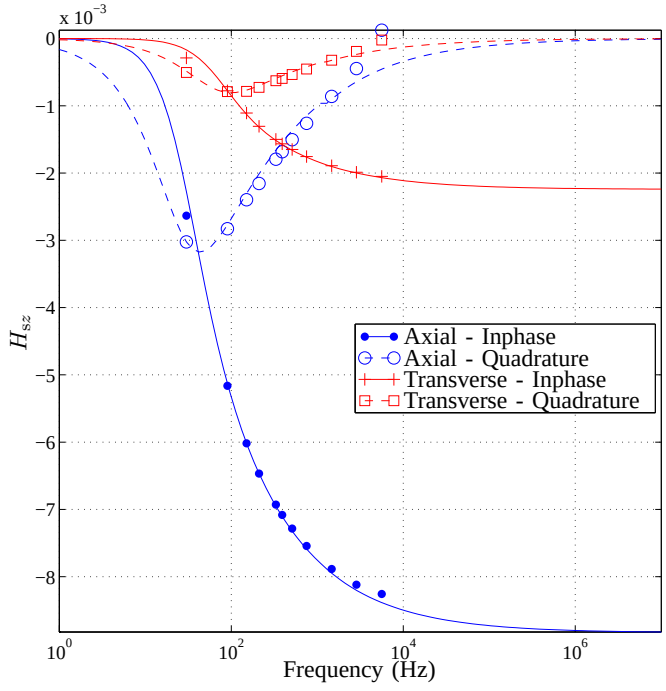

Fig. 12. Comparison of $H_{sz,d}$ from oblate aluminum spheroid A7 with combined model outlined in Sections II and III. Both axial and transverse cases. Optimized conductivity was $\sigma = 3.147\times10^7 \mho/m$.

field (see Section IV-B), objects closer than one or two characteristic lengths from the instrument may have important interaction with $m \geq 2$ orders of the primary field. For objects this close, our model may not accurately predict the induced field response unless the response due to higher order terms are included.

The exact permeability (for the steel) and conductivity of the spheroids were not known or measured beforehand. We sidestepped this lack of information by obtaining these parameters via inversion of the measurements. In other words, we extracted σ and μ_r using a simple search routine by fitting out model to the axial measurements first. We then used these extracted parameters for the transverse measurements from the same object and found them to deliver reasonable results. The resulting conductivity and permeability are within acceptable ranges for these metals.

The experimental GEM-3 we used for these measurements records reliable data at frequencies up to about 12kHz [31]. Measurements are not absolutely calibrated with respect to the primary field. Therefore, the following procedure to normalize and remove any possible constant offset was adopted. Let $H_{sz,d}$ be the z-component of the induced magnetic field measured with the GEM-3 and let H_z be the z-component of the induced magnetic field predicted by our model. In order to compare $H_{sz,d}$ and H_{sz} (as in Figs. 9–12), we set

$$H_{sz,d} = \left[\left(H_{sz,d} - \overline{H_{sz,d}}\right) \frac{\sum_f \left(\left|H_{sz} - \overline{H_{sz}}\right|\right)}{\sum_f \left(\left|H_{sz,dat} - \overline{H_{sz,dat}}\right|\right)} \right] + \overline{H_{sz}} \tag{21}$$

where the overline implies an average over frequency, and the summation is over all data frequencies used.

Data and model predictions are seen to agree quite well under all conditions except possibly for high frequencies where the accuracy of the data may be suspect [31]. The agreement is not as good for the cases comparing oblate spheroids. This may be due to not having the globally optimal σ and/or μ_r for the these spheroids or due to our truncation of (1) and (6) at $m = 1$.

V. Conclusion

We have constructed a broadband solution for the induced magnetic field from conducting and permeable prolate and oblate spheroids under time harmonic excitation in the magnetoquasistatic regime. Our combined method consists of the exact analytical solution, an asymptotic-assisted analytical solution, and a small penetration approximation (SPA). This combined solution is accurate to within 5% error for most spheroids with aspect ratio $\frac{1}{8} < e < 8$. Results produced by this combined method were compared to results from a finite element/boundary integral numerical method and found to be in excellent agreement. Results were also compared to induced magnetic field measurements taken by the UWB GEM-3 instrument from metal prolate and oblate spheroids. If the permeability and conductivity of the spheroids is allowed to vary within accepted physical ranges, results were seen to match very well with measurements. Using this model, one can calculate the broadband induced magnetic field response from a flexible set of canonical shapes such as spheres, spheroids, plates, and needles is now possible. The results indicate that

solutions from our model display distinct, systematic response patterns based on the spheroidal characteristics and orientation. On this basis, our method could become a forward model upon which inversions schemes may be based.

REFERENCES

[1] M. N. Nabighian, "Quasi-static transient response of a conducting permeable sphere in a dipolar field," *Geophysics*, vol. 35, no. 2, pp. 303–9, April 1970.

[2] S. E. Hjelt, "Regional em studies in the 1980's," *Surveys in Geophysics*, vol. 9, no. 3–4, pp. 349–87, Sept.–Dec. 1987.

[3] H. A. Haus and J. R. Melcher, *Electromagnetic Fields and Energy*. Englewood Cliffs, New Jersey: Prentice Hall, 1989.

[4] I. J. Won, D. A. Keiswetter, and T. H. Bell, "Electromagnetic induction spectroscopy for clearing landmines," *IEEE Trans. on Geoscience and Remote Sensing*, vol. 39, no. 4, pp. 703–709, April 2001.

[5] D. A. Keiswetter, W. A. SanFilipo, I. J. Won, J. M. Miller, T. H. Bell, E. R. Cespedes, and K. O'Neill, "Discriminating capabilities of multifrequency EMI data," *Proceedings of the SPIE The International Society for Optical Engineering*, pp. 130–40, 2000.

[6] N. Geng, P. Garber, L. Collins, L. Carin, D. Hansen, D. Keiswetter, and I. J. Won, "Wideband electromagnetic induction for metal target identification: theory, measurement, and signal processing," *Proceedings of the SPIE The International Society for Optical Engineering*, pp. 42–51, 1998.

[7] K. Sun, K. O'Neill, F. Shubitidze, S. A. Haider, and K. D. Paulsen, "Simulation of electromagnetic induction scattering from targets with negligible to moderate penetration by primary fields," *IEEE Trans. on Geoscience and Remote Sensing*, vol. 40, no. 4, pp. 910–27, April 2002.

[8] B. Johnson, T. G. Moore, B. J. Blejer, C. F. Lee, T. P. Opar, S. Ayasli, and C. A. Primmerman, "A research and development strategy for unexploded ordnance sensing," *Lincoln Laboratory Project Report, EMP-1*, April 1996.

[9] P. Wiseman, "30-year-old bombs still very deadly in laos," USA Today, p. 10A, December 12 2003.

[10] I. C. of the Red Cross. (2004) Raising awareness of mines and unexploded ordnance (uxo). [Online]. Available: http://www.icrc.org/Web/eng/siteeng0.nsf/htmlall/section_mine_and_uxo_a%wareness

[11] T. S. E. Research and D. P. (SERDP). (2004) Uxo projects. [Online]. Available: http://www.serdp.org/research/UXO.html

[12] J. R. Wait, "A conducting sphere in a time varying magnetic field," *Geophysics*, vol. 16, pp. 666–672, 1951.

[13] ——, "A conducting permeable sphere in the presence of a coil carrying an oscillating current," *Can. J. Phys.*, vol. 31, pp. 670–678, 1953.

[14] C. O. Ao, H. Braunisch, K. O'Neill, , and J. A. Kong, "Quasi-magnetostatic solution for a conducting and permeable spheroid with arbitrary excitation," *IEEE Trans. on Geoscience and Remote Sensing*, vol. 40, no. 4, pp. 887–97, April 2002.

[15] H. Braunisch, C. O. Ao, K. O'Neill, and J. A. Kong, "Magnetoquasistatic response of conducting and permeable spheroid under axial excitation," *IEEE Trans. on Geoscience and Remote Sensing*, vol. 39, no. 12, pp. 2689–2701, December 2001.

[16] B. E. Barrowes, K. O'Neill, T. M. Grzegorczyk, and J. A. Kong, "Asymptotic expansions of the prolate angular spheroidal wave function for complex size parameter," *Studies in Applied Mathematics*, Oct. 2003, submitted for publication.

[17] C. E. Baum, Ed., *Detection and Identification of Visually Obscured Targets*. Philadelphia, PA: Taylor & Francis, 1999.

[18] C. D. Moss, K. O'Neill, T. M. Grzegorczyk, and J. A. Kong, "A hybrid time domain model of electromagnetic induction from conducting, permeable targets," *IEEE Trans. on Geoscience and Remote Sensing*, to be submitted.

[19] I. J. Won, D. A. Keiswetter, D. Hansen, E. Novikova, and T. M. Hall, "Gem-3: a monostatic broadband electromagnetic induction sensor," *Jour. Envir. Eng. Geophysics*, vol. 2, no. 1, pp. 53–64, 1997.

[20] M. Abramowitz and I. A. Stegun, *Handbook of Mathematical Functions*, 9th ed. Dover Publications, Inc., 1970.

[21] C. Flammer, *Spheroidal Wave Functions*. Stanford: Stanford University Press, 1957.

[22] B. G. C. Hunter, "The eigenvalues of the angular spheroidal wave-equation," *Studies in Applied Mathematics*, vol. 66, no. 3, pp. 217–240, 1982.

[23] T. Do-Nhat, "Asymptotic expansion of the Mathieu and prolate spheroidal eigenvalues for large parameter c," *Canadian Journal of Physics*, vol. 77, no. 8, pp. 635–652, aug 1999.

[24] ——, "Asymptotic expansions of the oblate spheroidal eigenvalues and wave functions for large parameter c," *Canadian Journal of Physics*, vol. 79, no. 5, pp. 813–31, May 2001.

[25] A. Erdélyi, Ed., *Higher transcendental functions*, ser. Bateman Manuscript Project. New York: McGraw-Hill, 1953–55.

[26] J. W. Miles, "Asymptotic approximations for prolate spheroidal wave functions," *Studies in Applied Mathematics*, vol. 54, no. 4, pp. 315–49, Dec. 1975.

[27] K. Sun, K. O'Neill, I. Shamatava, and F. Shubitidze, "Application of prolate spheroid solutions in simulation of emi scattering with realistic sensors and objects." ACES conference, Mar. 2003, pp. 531–537.

[28] L. Tsang, J. A. Kong, and K. H. Ding, *Scattering of Electromagnetic Waves: Theories and Applications*. Wiley-Interscience, 2000.

[29] J. A. Stratton, *Electromagnetic Theory*. McGraw-Hill Book Company, Inc., 1941.

[30] R. Harrington, *Time-Harmonic Electromagnetic Fields*. McGraw-Hill Book Company, Inc., 1961.

[31] Personal communication with Geophex, December 2003.

Benjamin E. Barrowes received both his B.S. and M.S. degrees in Electrical Engineering from Brigham Young University in 1999, and the Ph.D. degree from the Massachusetts Institute of Technology, Cambridge in 2004. His research interests include wind-wave interaction, electromagnetic wave scattering from the sea surface and from random media. Additional interests include nanoscale energy generation techniques, computer interface methodologies, and electromagnetic induction models for nonspherical geometries specifically with regard to unexploded ordnance detection.

Kevin O'neill received the B.A. degree (magna cum laude) from Cornell University, Ithaca, NY, and the M.A., M.S.E., and Ph.D. degrees from Princeton University, Princeton, NJ. After an NSF post-doctoral fellowship at the Thayer School of Engineering at Dartmouth College, Hanover, NH, and the U.S. Army Cold Regions Research and Engineering Laboratory (CRREL), he joined CRREL as a Research Civil Engineer. His research has focused on numerical modeling of porous media transport phenomena and of geotechnically relevant electromagnetic problems. He has been a Visiting Fellow in the Department of Agronomy at Cornell University, continues as a Visiting Scientist at the Center for Electromagnetic Theory and Applications at the Massachusetts Institute of Technology, Cambridge, and since 1984 has been on the adjunct faculty of the Thayer School. Current work centers on electromagnetic remote sensing of surfaces, layers, and especially buried objects such as unexploded ordnance.

Tomasz M. Grzegorczyk received his PhD thesis from the Laboratoire d'Electromagnétisme et d'Acoustique (LEMA) in December 2000. His research activities concerned the modeling of millimeter and submillimeter structures using numerical methods, as well as their technological realizations with the use of micromachining techniques. In January 2001, he joined the Research Laboratory of Electronics (RLE), Massachusetts Institute of Technology (MIT), USA, where he is now a research scientist. His research interests involve the polarimetric study of ocean and forest, electromagnetic induction from spheroidal object for unexploded ordnances modeling, waveguide and antenna design, wave propagation over rough terrains and study of left-handed media.

Xudong Chen received B.S. and M.S. degrees in Electrical Engineering in 1999 and 2001 from Zhejiang University, Hangzhou, China. His research interests include electromagnetic inverse problem and mathematical modeling. He won first prize in the Chinese National Mathematical Contest in Modeling in 1997. Since September, 2001, he has been a research assistant with the Center for Electromagnetic Theory and Application (CETA) group in the Research Laboratory of Electronics (RLE), Massachusetts Institute of Technology (MIT).

Jin A. Kong received the Ph.D. degree from Syracuse University, Syracuse, NY, in 1968. He is the President of The Electromagnetics Academy and Professor of Electrical Engineering at the Massachusetts Institute of Technology, Cambridge, where he is also the Chairman of Area IV on Energy and Electromagnetic Systems in the Department of Electrical Engineering and Computer Science and Director of the Center for Electromagnetic Theory and Applications in the Research Laboratory of Electronics. His research interest is in the area of electromagnetic wave theory and applications. He has published over 30 books including Electromagnetic Wave Theory (New York: Wiley-Interscience, 1975, 1986, 1990; EMW Publishing since 1998) and over 600 refereed journal articles, book chapters, and conference papers. He has been principal investigator for more than 100 grants and contracts from various government agencies and industry. He has served as consultant, external examiner, and advisor to industry, academia, national governments, and the United Nations. He has been reviewer for many journals, book companies, and government agencies, and served as session chairman, organizer, and member of advisory and technical program committees for numerous international and national conferences and symposia, including serving as Chairman for the Progress In Electromagnetics Research Symposium (PIERS) since 1989. He is Editor for the Wiley Series in Remote Sensing, Editor-in-Chief of the Journal of Electromagnetic Waves and Applications (JEMWA), and Chief Editor for the book series Progress In Electromagnetics Research (PIER). Dr. Kong received the S. T. Li Prize and the Distinguished Achievement Award from the IEEE Geoscience and Remote Sensing Society in 2000.